ISSN 1674-1056
http://cpb.iphy.ac.cn
http://iopscience.iop.org/cpb
中国物理 B
Chinese Physics
中国物理 Chinese Physics B

In-situ TEM observation of the evolution of helium bubbles in Mo during He^+ irradiation and post-irradiation annealing

Yi-Peng Li(李奕鹏), Guang Ran(冉广), Xin-Yi Liu(刘歆翌), Xi Qiu(邱玺), Qing Han(韩晴), Wen-Jie Li(李文杰), and Yi-Jia Guo(郭熠佳)

Citation: Chin. Phys. B, 2021, 30 (**8**): 086109. DOI: 10.1088/1674-1056/abff48
Journal homepage: http://cpb.iphy.ac.cn; http://iopscience.iop.org/cpb

What follows is a list of articles you may be interested in

Microstructure evolution of T91 steel after heavy ion irradiation at 550 ℃

Ligang Song(宋力刚), Bo Huang(黄波), Jianghua Li(李江华), Xianfeng Ma(马显锋), Yang Li(李阳), Zehua Fang(方泽华), Min Liu(刘敏), Jishen Jiang(蒋季伸), and Yanying Hu(胡琰莹)
Chin. Phys. B, 2021, 30 (**8**): 086103. DOI: 10.1088/1674-1056/ac0a64

Evolution of helium bubbles in nickel-based alloy by post-implantation annealing

Rui Zhu(朱睿), Qin Zhou(周钦), Li Shi(史力), Li-Bin Sun(孙立斌), Xin-Xin Wu(吴莘馨), Sha-Sha Lv(吕沙沙), and Zheng-Cao Li(李正操)
Chin. Phys. B, 2021, 30 (**8**): 086102. DOI: 10.1088/1674-1056/ac0783

Effect of helium concentration on irradiation damage of Fe-ion irradiated SIMP steel at 300 ℃ and 450 ℃

Zhen Yang(杨振), Junyuan Yang(杨浚源), Qing Liao(廖庆), Shuai Xu(徐帅), and Bingsheng Li(李炳生)
Chin. Phys. B, 2021, 30 (**5**): 056107. DOI: 10.1088/1674-1056/abd6f9

Extended damage range of $(Al_{0.3}Cr_{0.2}Fe_{0.2}Ni_{0.3})_3O_4$ high entropy oxide films induced by surface irradiation

Jian-Cong Zhang(张健聪), Sen Sun(孙森), Zhao-Ming Yang(杨朝明), Nan Qiu(裘南), Yuan Wang(汪渊)
Chin. Phys. B, 2020, 29 (**6**): 066104. DOI: 10.1088/1674-1056/ab8374

Effect of microstructure on ^{3}He migration in $TiT_{1.9}$ films

Haifeng Wang(王海峰), Shuming Peng(彭述明), Wei Ding(丁伟), Huahai Shen(申华海), Weidu Wang(王维笃), Xiaosong Zhou(周晓松), Xinggui Long(龙兴贵)
Chin. Phys. B, 2018, 27 (**9**): 096103. DOI: 10.1088/1674-1056/27/9/096103

SPECIAL TOPIC — Ion beam modification of materials and applications

In-situ TEM observation of the evolution of helium bubbles in Mo during He^+ irradiation and post-irradiation annealing*

Yi-Peng Li(李奕鹏)[1,2], Guang Ran(冉广)[1,2,†], Xin-Yi Liu(刘歆翌)[1,2], Xi Qiu(邱玺)[3], Qing Han(韩晴)[1,2], Wen-Jie Li(李文杰)[3], and Yi-Jia Guo(郭熠佳)[1,2]

[1] *College of Energy, Xiamen University, Xiamen* 361102, *China*

[2] *Fujian Research Center for Nuclear Engineering, Xiamen* 361102, *China*

[3] *Science and Technology on Reactor System Design Technology Laboratory, Nuclear Power Institute of China, Chengdu* 610213, *China*

(Received 15 April 2021; revised manuscript received 6 May 2021; accepted manuscript online 10 May 2021)

The evolution of helium bubbles in purity Mo was investigated by *in-situ* transmission electron microscopy (TEM) during 30 keV He^+ irradiation (at 673 K and 1173 K) and post-irradiation annealing (after 30 keV He^+ irradiation with the fluence of 5.74×10^{16} He^+/cm^2 at 673 K). Both He^+ irradiation and subsequently annealing induced the initiation, aggregation, and growth of helium bubbles. Temperature had a significant effect on the initiation and evolution of helium bubbles. The higher the irradiation temperature was, the larger the bubble size at the same irradiation fluence would be. At 1173 K irradiation, helium bubbles nucleated and grew preferentially at grain boundaries and showed super large size, which would induce the formation of microcracks. At the same time, the geometry of helium bubbles changed from sphericity to polyhedron. The polyhedral bubbles preferred to grow in the shape bounded by {100} planes. After statistical analysis of the characteristic parameters of helium bubbles, the functions between the average size, number density of helium bubbles, swelling rate and irradiation damage were obtained. Meanwhile, an empirical formula for calculating the size of helium bubbles during the annealing was also provided.

Keywords: helium bubbles, *in-situ* TEM observation, ion irradiation, annealing, molybdenum

PACS: 61.80.−x, 61.80.Jh, 68.37.Lp, 61.82.Bg **DOI:** 10.1088/1674-1056/abff48

1. Introduction

Based on its excellent high temperature strength, high melting point, and good thermal conductivity, molybdenum (Mo) is a promising candidate material for innovative nuclear power systems such as fast neutron reactor, thorium-fueled molten salt reactor, fusion reactor, and space nuclear reactor.[1–3] However, in the irradiation environment, the collision of energic particles (neutrons, fission products, transmutation products, γ rays, α rays, etc.) with atoms in Mo lattice produces basic crystal defects including vacancies and interstitials, causing irradiation damage.[4–8] Meanwhile, hydrogen and helium generated in Mo will accelerate the deterioration of its irradiation resistance, especially helium. Helium is insoluble in virtually all materials due to its closed-shell electronic configuration and easily combination with vacancy to form helium–vacancy clusters such as He_2V_2, He_3V_2, and more complex He_nV_m (the range of n and m inside the cluster is from 1 to the possible maximum number of defect species).[9,10] The helium accumulation in Mo regarded as plasma facing materials in fusion reactor mainly comes from the injection of helium ash (the products of D-T fusion reaction) and the (n, α) transmutation reaction.[11] Under the action of thermal effect and cascade collision, helium–vacancy clusters will evolve into helium bubbles and simultaneously emit interstitials to form dislocation loops, which will lead to irradiation swelling, hardening, and embrittlement, and increase tritium retention.[12–16] Meanwhile, helium irradiation can lead to the transformation of materials from crystal to amorphous.[17] Therefore, it is of great significance for the practical application of molybdenum and the development of irradiation damage theory to study the evolution and mechanism of helium bubbles under the conditions of cascade collision and thermal effect.

As a hot topic, the evolution of helium bubbles during He^+ irradiation or post-implantation annealing has been *in-situ* studied in recent years.[18–21] Ono *et al.*[18] studied the formation and migration of helium bubbles in Fe and Fe-9Cr ferritic alloys using *in-situ* TEM observation. El-Atwani *et al.*[19] and Yi *et al.*[20] investigated the effects of irradiation parameters (such as temperature and helium fluence) on the evolution of helium bubbles in tungsten through *in-situ* helium irradiation. The results[18–20] show that the size, density, shape, and distribution of helium bubbles are affected by multiple factors, such as irradiation temperature and irradiation dose. Uniform distribution of helium bubbles presents in the matrix under low temperature irradiation, while gas bubbles mainly nucleate at grain boundaries and dislocation lines under high temperature

*Project supported by the National Natural Science Foundation of China (Grant Nos. U1967211, U1832112, and 11975191).

†Corresponding author. E-mail: gran@xmu.edu.cn

© 2021 Chinese Physical Society and IOP Publishing Ltd

irradiation. In addition, Chen *et al.*[21] carried out an *in-situ* annealing experiment on the pre-irradiated FeCrAl alloy to research the growth, migration, and coalescence of helium bubbles, and believed that the migration and coalescence of small bubbles were controlled by the surface diffusion mechanism. However, the evolution difference of helium bubbles (including nucleation, growth, distribution, morphology, etc.) during *in-situ* irradiation and post-implantation *in-situ* annealing needs to be further investigated. In fact, this kind of comparative study is also required in other energetic particle irradiation (such as electron irradiation[22]). Furthermore, a common feature of bubble evolution at high temperature is the formation of nonspherical polyhedral geometry.[19,23–25] It is known that in the He-implanted body centered cubic (BCC) materials (such as W,[19] Nb,[24] and Fe-9Cr alloy[25]), the bubble will take on the shape of a uniaxial polyhedron. However, the detailed configuration of bubble and the orientation relationship between bubble and material matrix still need to be studied in detail.

Meanwhile, as defect sinks, grain boundaries and interfaces play an important role in suppressing or controlling irradiation damage,[26–28] and the strain field obviously affects the defect formation energy and threshold displacement energy.[29] In the process of irradiation or annealing, interstitial helium atoms or helium-vacancy clusters can reach the grain boundary through diffusion, thus promoting the formation of large-size bubbles at grain boundary.[30] El-Atwani *et al.*[31] found that the effective diffusion length of helium atoms or their related defects in nanocrystalline materials to grain boundaries was shortened, which aggravated the formation of grain boundary bubbles. They also found that the tungsten grain boundary showed the formation of preferential bubble at 1223 K, and the bubbles at the grain boundary were larger than those in the grain matrix.[19] Therefore, it is important to understand the size, distribution, and evolution of helium bubbles at grain boundaries.

In the current study, the *in-situ* 30 keV He^+ irradiation experiments were carried out at 673 K and 1173 K to study the effects of irradiation temperature on the growth and evolution of helium bubbles, while *in-situ* annealing experiments were carried out on the Mo pre-irradiated by 30 keV He^+ to the fluence of 5.74×10^{16} He^+/cm^2 at 673 K. It should be noted that although the amount of helium produced in Mo is small in actual service, in order to obtain the obvious evolution behavior and related mechanism of helium bubbles, we increased the helium fluence in the irradiation experiment. The different growth behaviors of helium bubbles during *in-situ* irradiation and *in-situ* annealing process were characterized and summarized. Meanwhile, the formation of polyhedral helium bubbles at high temperature and the preferential aggregation of helium bubbles at grain boundaries and their possible effects on the properties of Mo were discussed.

2. Experimental procedure

2.1. TEM sample preparation

Pure Mo (99.99% purity) TEM samples with 3 mm diameter were prepared by twin-jet electropolishing using a mixed solution with 70 mL sulphuric acid and 350 mL methanol at 258 K. The detailed preparation of TEM samples could be found in our published paper.[32]

2.2. *In-situ* He^+ irradiation

In-situ 30 keV He^+ irradiation was performed at the Xiamen Multiple Ion Beam *In-situ* TEM Analysis Facility (XIAMEN Facility)[33] and its detailed irradiation process has been reported in our published paper.[32] In the present work, we mainly focused on the evolution of helium bubbles during He^+irradiation, which is different from our published paper that reported the characteristics and evolution of dislocation loops. Details of damage profile and helium concentration profile were calculated by the SRIM[34] (Stopping and Ranges of Ions in Matter) program in quick Kinchin–Pease mode with normal incidence angle and the displacement energy (E_d) of 60 eV for Mo[35] as shown in Fig. 1(a). The irradiation temperatures of 673 K and 1173 K were controlled by Gatan 652 double-tilt heating stage with a water-cooling system. In the process of irradiation, the temperature fluctuation range was less than 0.5 K. The thicknesses of the *in-situ* monitored region obtained by convergent beam electron diffraction were about 105 nm and 80 nm at 673 K and 1173 K irradiation, respectively. The average irradiation dose rate, injected helium concentration rate, and other detailed irradiation parameters are shown in Table 1. Time profiles of the displacement damage and injected helium concentration at the monitored region are shown in Fig. 1(b). Therefore, it was easy to obtain the total irradiation damage and injected He^+ concentration at any irradiation time. To make sure that He^+ irradiated TEM sample vertically, the electron beam was shut down and the sample was tilted to 68° to be perpendicular to the helium beam. After irradiation with a certain helium fluence, we stopped He^+ beam, tilted the TEM sample to be perpendicular to the electron beam, then turned on the electron beam and finally took TEM images as soon as possible to minimize the annealing effect.

2.3. *In-situ* annealing experiment

After irradiation with the fluence of 5.74×10^{16} He^+/cm^2 at 673 K, the He^+ beam was turned off, and then the irradiated Mo TEM sample was *in-situ* annealed at the Gatan 652 heating holder. The TEM sample was sequentially annealed for 25 min at 773 K, 873 K, and 973 K. At any annealing temperature, TEM images were captured every 5 min. The detailed annealing parameters are shown in Fig. 1(c).

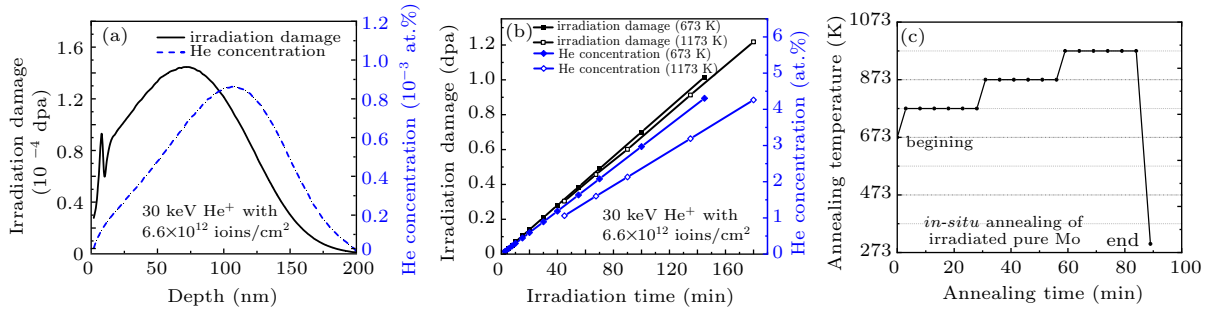


Fig. 1. (a) Depth profiles of the displacement damage and injected He^+ concentration in pure Mo irradiated by 30 keV He^+ with a fluence of 6.6×10^{12} ions/cm^2 calculated by SRIM program in quick Kinchin–Pease mode. (b) Time profiles of the displacement damage and injected He concentration. (c) *In-situ* annealing sketch (temperature vs. time) of irradiated Mo TEM sample.

2.4. TEM images taken

Under-focus TEM images were taken during *in-situ* helium irradiation and *in-situ* annealing and used to analyze the characteristic change of helium bubbles. In the under-focus images, helium bubbles are shown as white spots with black streaks. It should be noted that we did not take the temperature down to room temperature (RT) during the characterization steps in the *in-situ* helium irradiation experiment and *in-situ* annealing experiment. In the process, we tried to reduce the time of taking images as much as possible. In general, a group of TEM images were taken in less than one minute at a specific irradiation time point or annealing time point. Helium bubbles were counted by a manual bubble-by-bubble counting in Gatan Digital Micrograph software, which was used to calculate the average size and volume number density of the formed helium bubbles in the monitored region.

Table 1. The parameters of the *in-situ* 30 keV He^+ irradiation.

	Irradiation temperature (K)	Thickness of the monitored region (nm)	Injected He^+ flux (ions/cm^2·s)	Average damage rate (dpa/s)	Average He concentration rate (at.%/s)	Total irradiation time (min)	Total irradiation dose (dpa)	Total He concentration (at.%)
I	673	105	6.6×10^{12}	1.17×10^{-4}	4.95×10^{-4}	145	1.02	4.31
II	1173	80	6.6×10^{12}	1.13×10^{-4}	3.94×10^{-4}	180	1.22	4.26

3. Results

3.1. *In-situ* He^+ irradiation at 673 K

In the process of He^+ irradiation, with the accumulation of helium atoms and vacancies, helium bubbles will eventually form, which will not only cause swelling and hardening but also act as strong trapping sites for tritium and then increase the tritium retention in materials. Figure 2 shows the evolution of helium bubbles in the Mo irradiated *in-situ* by 30 keV He^+ at 673 K. The incident direction of He^+ beam is perpendicular to the paper surface, and all images have the same magnification. Figure 2(a) shows the microstructure captured under strong two-beam condition using the diffraction vector $\boldsymbol{g} = 110$ close to [001] zone axis before irradiation, which indicates that there are not any possibly obvious defects, such as voids or dislocation loops. Because the TEM sample was prepared by twin-jet electropolishing, an unstressed thin area with dozens of micron size was obtained, ensuring that the monitored area has a better chance of surviving defects under the conditions of high temperature and long He^+ irradiation time. The black stripe in the upper left corner of the micrograph is the grain boundary.

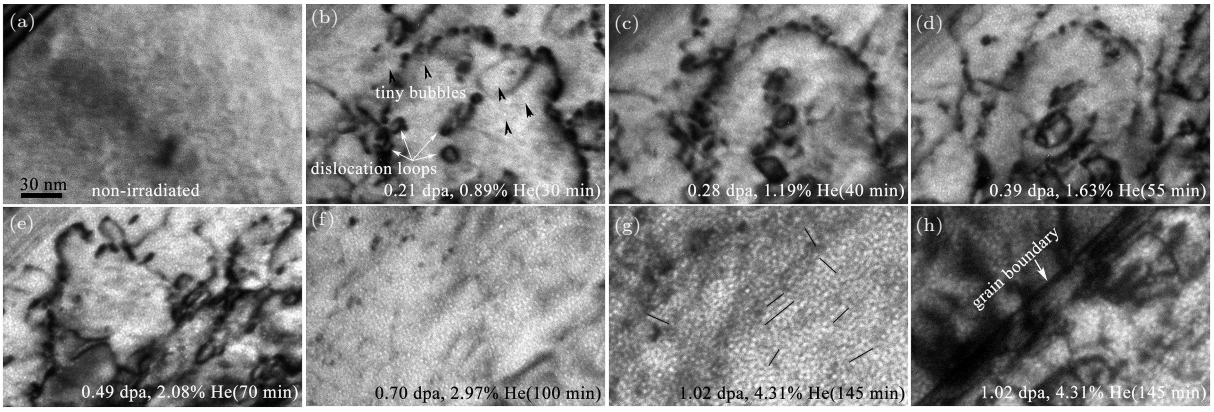


Fig. 2. Under-focus TEM images showing the *in-situ* evolution of helium bubbles in the Mo irradiated by 30 keV He^+ with a flux of 6.6×10^{12} ions/(cm^2·s) at 673 K. The helium concentrations are (a) 0.0%; (b) 0.89%; (c) 1.19%; (d) 1.63%; (e) 2.08%; (f) 2.97%; (g) 4.31%; and (h) 4.31%. Images (g) and (h) are the different regions after the same helium ion irradiation. All images have the same scale bar.

With the accumulation of He^+ irradiation fluence, the helium concentration in the monitored region with approximately 105 nm thickness reaches 0.89 % after irradiation with the fluence of 1.19×10^{16} ions/cm^2. Helium bubbles with obvious size can be observed, which are indicated by black arrows in the under-focus TEM image (Fig. 2(b)). The average size of helium bubbles is 1.4 nm. The reason why no obvious helium bubbles can be seen before is that the size of small bubbles is below the resolution of TEM observation during He^+ irradiation, and only the bubbles with the scale of more than 1 nm can be easily distinguished, which should be attributed to that the mechanical micro-vibration induced by the vacuum pump attached to the *in-situ* irradiation facility and the thermal vibration of the TEM sample at high temperature irradiation cause the decrease of TEM resolution.

It is worth noting that helium bubbles in the initial stage of He^+ irradiation concentrate near the dislocations, which is attributed to that the dislocations are strong sinks absorbing irradiation-induced defects such as interstitials, vacancies, and small-size defect clusters. Therefore, helium bubbles are easy to initiate and grow here. These phenomena were also found in both pure Fe and SVRAM low activation steels,[36] which showed that the dislocations could promote the trapping and aggregation of helium atoms and vacancies to form helium bubbles. With the continuous accumulation of injected helium fluence, helium bubbles continue to grow. The size of helium bubbles increases slowly from 1.4 nm to 2.3 nm when the helium fluence increases from 0.89 % to 4.31 % in the monitored region. The average size increases only 0.9 nm from visible helium bubbles to the end of irradiation. In general, the bubbles are uniformly distributed in the molybdenum matrix (Fig. 2(f)). Although the bubble size near the grain boundary is slightly larger than that inside the grain (Figs. 2(e) and 2(h)), the bubble size is still small. This means that bubbles mainly nucleate and grow independently, and there is little aggregation and coalescence between bubbles. Meanwhile, with the increase of helium fluence, not only the bubble size increases, but also some helium bubbles are arranged in line shape, as indicated by the short black lines in Fig. 2(g).

The change of the average size of helium bubbles with the increase of injected helium fluence is shown in Fig. 3(a). Within the current irradiation fluence range, the growth of bubble size is approximately linear, and the growth rate is slow but stable. Figures 3(b)–3(g) show the frequency of size distribution of helium bubbles after different fluence irradiation. With the increase of irradiation fluence, the size distribution of helium bubbles has been relatively uniform, and the distribution range becomes large. The change trend of the whole distribution curve is moving to the high value, and the frequency height first rises and then decreases.

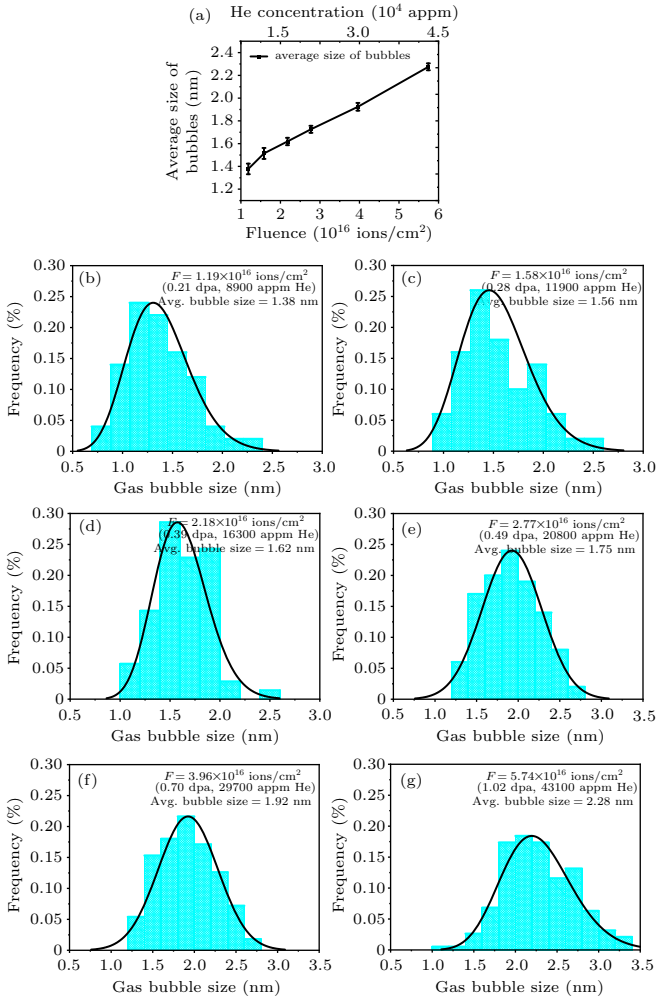


Fig. 3. (a) The relationship between the average size of helium bubbles and irradiation fluence at 673 K. (b)–(g) The frequency of size distribution of helium bubbles.

3.2. *In-situ* annealing after He^+ irradiation at 673 K

In the process of He^+ irradiation at 673 K, although the irradiation fluence finally reaches 5.74×10^{16} ions/cm^2, the size of helium bubble changes a little. During the process from the He^+ fluence of observable helium bubbles to the injected helium atoms with 4.31 at.% in the monitored region, the average size of helium bubbles increases by less than 1 nm. Therefore, to study the thermal effect on the growth of helium bubbles, the helium beam was stopped, and then the irradiated TEM sample was *in-situ* annealed. In the process, the behavior of bubble growth under different annealing temperature and time was researched by *in-situ* TEM observation. Figure 4 shows the *in-situ* TEM micrographs of the Mo sample annealed at different annealing experiment conditions.

After annealing at 773 K for 5 min (Fig. 4(b)), it can be seen that the shape and size of helium bubbles have no obvious change compared with that under ion irradiation. The statistical results show that the average size of helium bubbles increases from 2.3 nm after final irradiation to 2.5 nm after annealing at 773 K for 5 min. In general, the average size of

helium bubbles increases slowly at 773 K, although the annealing time is prolonged. For example, after annealing for 25 min, the average size of helium bubbles is only 2.8 nm. TEM images show that helium bubbles are distributed randomly in the Mo matrix, and the density does not change significantly. Figures 4(d) and 4(e) are the TEM images of helium bubbles in the Mo annealed at 873 K for 5 min and 25 min, respectively. The corresponding average sizes of helium bubbles are 3.0 nm and 3.3 nm, respectively, indicating that the size change of helium bubbles is still small. When the annealing temperature rises to 973 K, the average sizes of helium bubbles in Figs. 4(f) and 4(g) corresponding to 5 min and 25 min annealing are 3.6 nm and 4.0 nm, respectively. The size of helium bubbles increases slightly during annealing, but it is still not obvious. As a whole, the average size of helium bubbles increases from 2.3 nm after final irradiation to 4.1 nm after annealing at 973 K for 25 min, and the increase of helium bubble size is approximately 1.8 nm. It can be seen that the thermal effect leads to the increase of the helium bubble size, which can be attributed to the migration and aggregation of helium atoms, vacancies, and defect clusters formed by helium ion irradiation.

As indicated by the ellipses A1 and B1, the morphology of bubbles in the Mo sample annealed at 873 K for 25 min and annealed at 773 K for 5 min is very similar, except that the bubble size has a relative increase. However, after annealing at 973 K for 25 min, the bubbles grow and merge obviously. For example, the bubbles labeled by letters a_1 and a_2 in the ellipse A1 grow just a little bit under the annealing conditions from 773 K for 5 min (Fig. 5(a)) to 873 K for 25 min (Fig. 5(b)), but they merge to form the bubble a_4 (Fig. 5(c)). Meanwhile, during this annealing process, the bubble a_3 keeps growing independently and does not merge with other bubbles. Similarly, we observe that the bubbles b_1, b_2, b_3, b_4, and b_5 in the ellipse B1 (Fig. 5(b)) merge to form a large-sized bubble b_6 (Fig. 5(c)) after annealing at 973 K for 25 min.

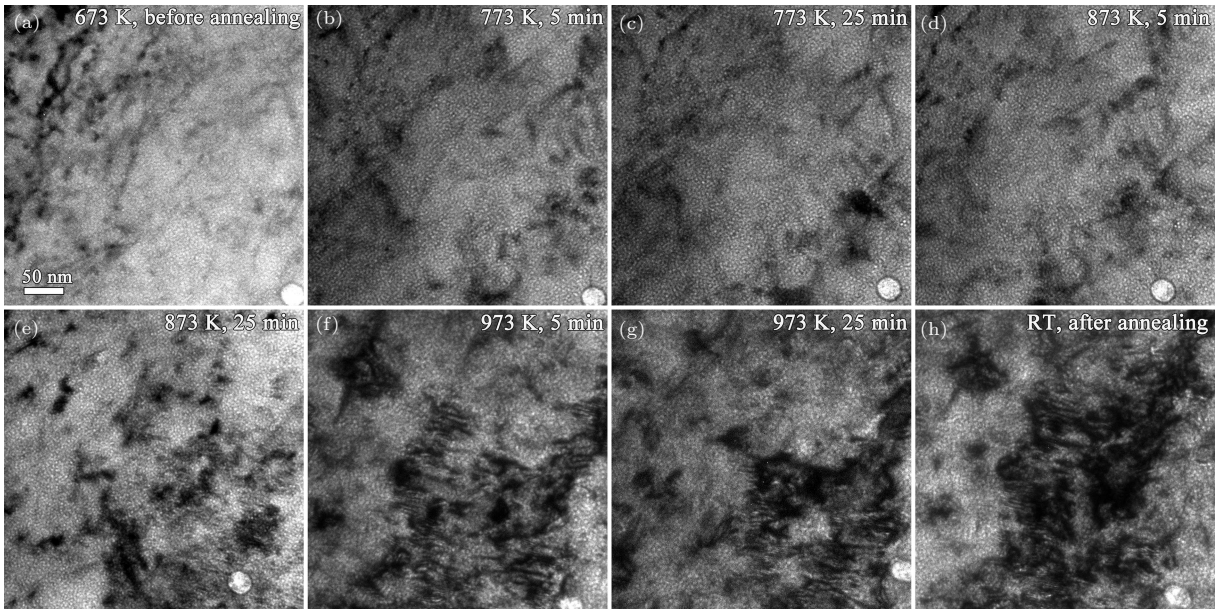


Fig. 4. *In-situ* TEM observation of the bubble evolution during annealing in the Mo pre-irradiated by 30 keV He^+ with a total fluence of 5.74×10^{16} ions/cm^2, (a) 673 K before annealing, (b) and (c) annealed at 773 K for 5 min and 25 min, respectively; (d) and (e) annealed at 873 K for 5 min and 25 min, respectively; (f) and (g) annealed at 973 K for 5 min and 25 min, respectively; (h) RT after annealing.

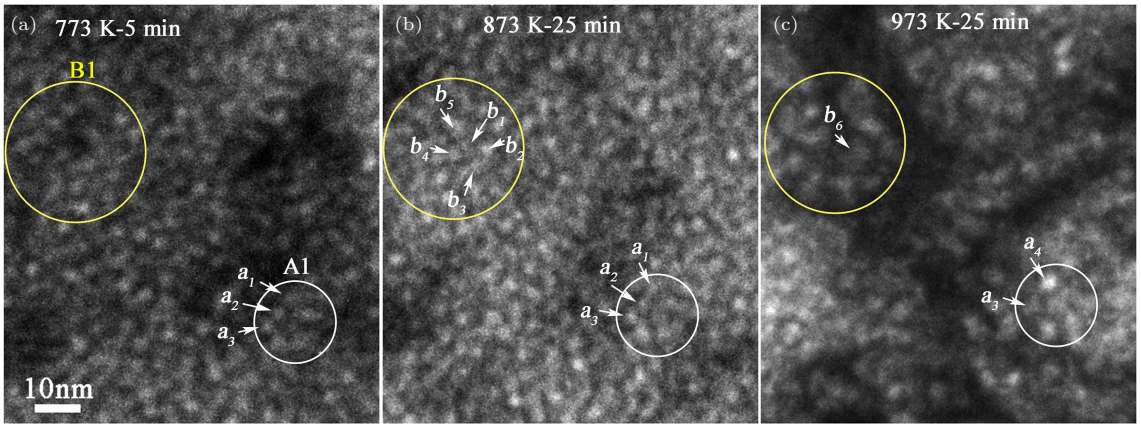


Fig. 5. *In-situ* TEM observation of the bubble evolution in the irradiated Mo, (a) annealed at 773 K for 5 min; (b) annealed at 873 K for 25 min; (c) annealed at 973 K for 25 min.

3.3. *In-situ* He^+ irradiation at 1173 K

From the above *in-situ* irradiation at 673 K and *in-situ* annealing at 973 K and below, it can be seen that the change of bubble size is small, which indicates that the temperature causing the significant increase of bubble size is still low. Therefore, *in-situ* helium irradiation was carried out at a higher temperature of 1173 K. Figure 6 shows the bright-field TEM images of the nucleation and evolution of helium bubbles induced by *in-situ* He^+ irradiation at 1173 K. Helium bubbles are almost hexagonal in shape. All these images were taken near the [111] zone axis. The rotation and offset of the crystal zone axis will change the shape of helium bubbles, which is caused by the different projections in different directions. The detailed analysis is presented in Section 4.3. The average size, volume number density, and size distribution of helium bubbles and swelling rate with the change of irradiation dose are quantitatively analyzed, as shown in Fig. 7. The relationship between helium bubble size r (the side length of cube) and the observed hexagon side length a can be regarded as $r = (2\sqrt{3}/3)a$. And the irradiation swelling rate caused by helium bubbles can be calculated by $\Delta V/V = (\sum_1^n r_i^3)/St$, where ΔV is the total volume change, n is the total number of helium atoms, S and t are the area and thickness of the monitored region, respectively. The thickness is approximately 80 nm.

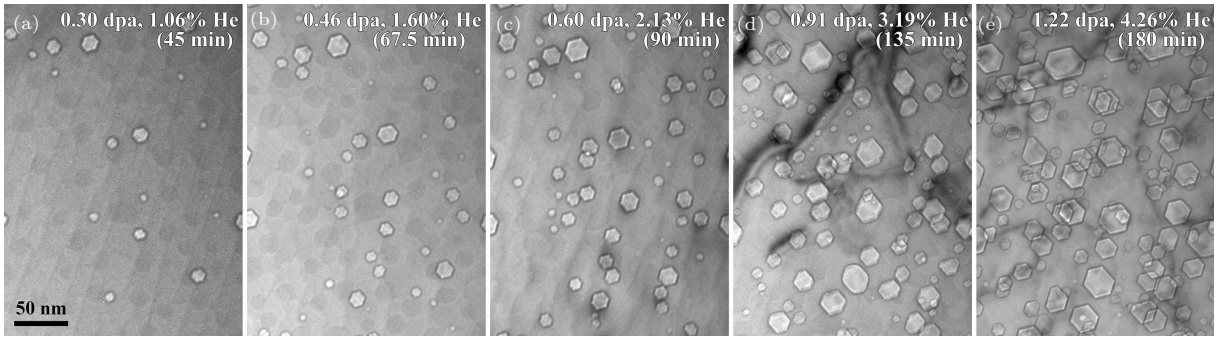


Fig. 6. *In-situ* bright-field TEM images of the nucleation and evolution of helium bubbles induced by He^+ irradiation at 1173 K. The helium concentrations were (a) 1.06%; (b) 1.60%; (c) 2.13%; (d) 3.19%; and (e) 4.26%. All the images were taken near the zone axis of [111] and have the same scale bar.

Combined with the *in-situ* evolution of helium bubbles in Fig. 6 and the statistical results in Fig. 7, it can be seen that the size and density of helium bubbles increase significantly with the increase of irradiation dose. When irradiated at 1173 K for 0.30 dpa (1.06% helium concentration), the average size of helium bubble is about 6.2 ± 2.1 nm, the maximum size is less than 10 nm, the bubble density is 3×10^{21} m^{-3}, and the swelling rate is about 0.1%; while at 1.22 dpa (4.26% helium concentration), the average size of helium bubble increases to 12.6 ± 4.4 nm, the maximum size approaches 25 nm, the bubble density increases to 2.1×10^{22} m^{-3}, and the swelling rate is approximately 5.8%.

Compared with the results of low-temperature *in-situ* irradiation and subsequent *in-situ* annealing experiments, we found that the size of helium bubbles under high-temperature irradiation increased dramatically, and the geometry of helium bubbles changed from sphericity to polyhedron. As shown in Fig. 8, the bright-field TEM images taken at different crystal zone axes show the different projection shapes of helium bubbles. The shapes of helium bubbles observed near the zone axes $Z = [111]$, $[001]$, and $[011]$ are approximately regular hexagon, square, and parallel hexagon, respectively. These observations are in good agreement with the projection of the cube near the corresponding crystal zone axis shown in the insets, which implies that the helium bubbles directly produced by He^+ irradiation at high temperature (1173 K) can be regarded as a regular cube structure.

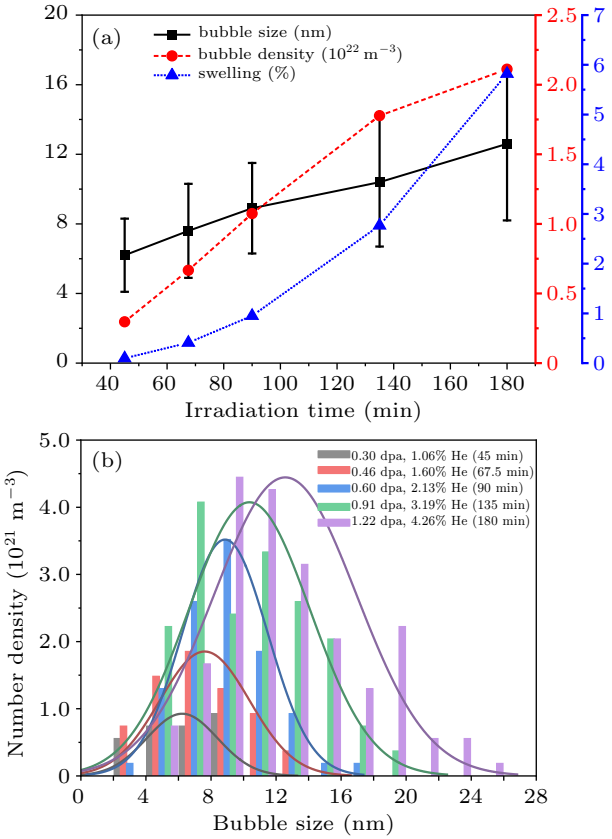


Fig. 7. (a) Average bubble size and number density of helium bubbles and swelling rate as the functions of irradiation damage in helium irradiated Mo at 1173 K. (b) The relationship between the number density and helium bubble size at different irradiation doses.

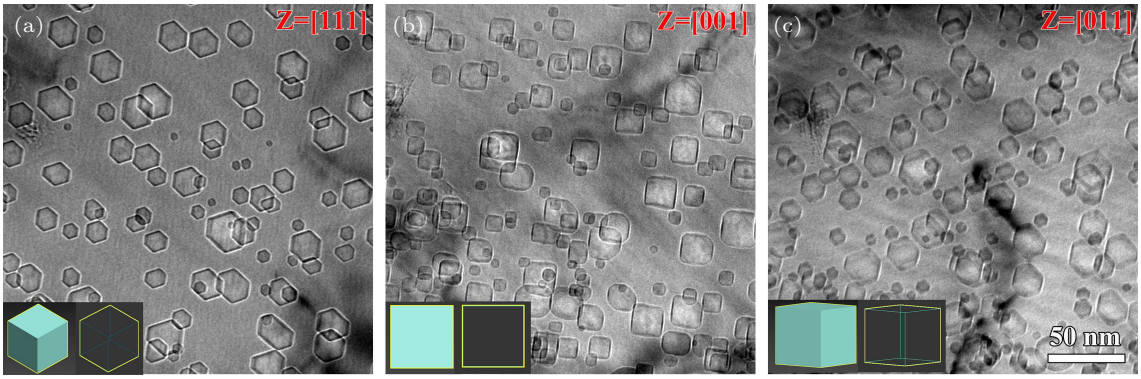


Fig. 8. Comparison of the bubble shape observed in the 1173 K irradiation with the projected shapes of cube (insets) near different zone axes: (a) [111], regular hexagon; (b) [001], square; and (c) [011], parallel hexagon.

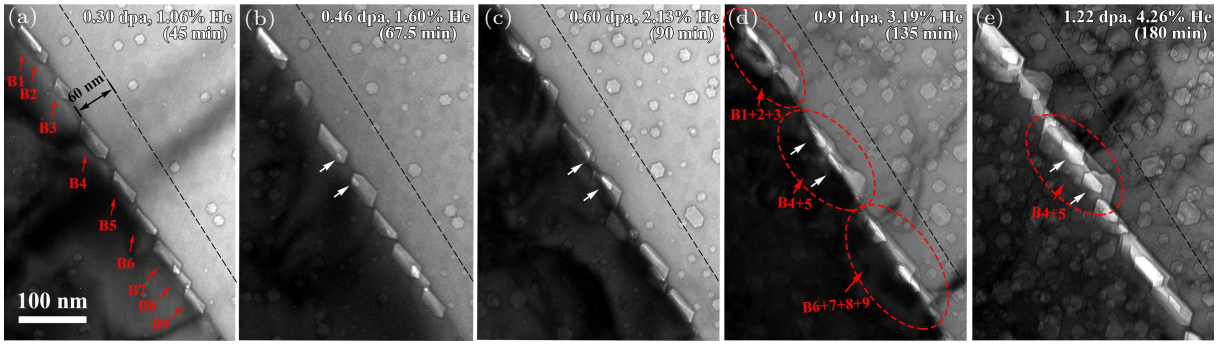


Fig. 9. *In-situ* bright-field TEM images showing the evolution of helium bubbles at grain boundary with the increase of He^+ irradiation fluence. The irradiation doses are (a) 0.3 dpa (1.06% helium); (b) 0.46 dpa (1.60% helium); (c) 0.60 dpa (2.13% helium); (d) 0.91 dpa (3.19% helium); and (e) 1.22 dpa (4.26% helium).

Figure 9 shows the characteristics and evolution of helium bubbles at grain boundary with the increase of He^+irradiation fluence. The size of helium bubbles distributed at grain boundary is much larger than that within grain. Moreover, the size difference becomes more and more significant with the irradiation. At the early stage of irradiation (≤ 0.46 dpa), a denudation zone with a width of about 50–60 nm is observed near the grain boundary, in which only a few small bubbles are found (Figs. 9(a) and 9(b)). With the increase of He^+irradiation fluence, the width of the denuded zone will decrease, and helium bubbles appear in this region gradually (Figs. 9(c)–9(e)). With the increase of He^+ fluence, the size of helium bubbles increases rapidly, especially those at the grain boundary. However, it is worth noting that the number of helium bubbles at the grain boundary is quite stable, and there is almost no new bubble nucleate, which indicates that the injected He atoms preferentially gather at the nucleated helium bubbles rather than newly nucleate independently. The coalescence of large-size helium bubbles occurs when the adjacent bubbles grow up and collide with each other. As shown in Fig. 9(d), nine side-by-side helium bubbles at the grain boundary collide, overlap, coalesce, and finally form three large-size helium bubbles, bubbles B1 + 2 + 3, B4 + 5, and B6 + 7 + 8 + 9. Subsequently, helium bubbles continue to grow, and the three large helium bubbles are coalesced or overlapped. The grain boundary in the observation region is completely covered by helium bubbles (Fig. 9(e)). The colliding helium bubbles are not simply connected, but will gradually merge into a regular shape, as shown in the shape evolution of bubble B4 + 5 in Figs. 7(d)–7(e). Moreover, the distribution of helium bubbles at the grain boundary may overlap, which is attributed to that helium bubbles nucleate at different depths. Two small-size bubbles pointed by the white arrows (Figs. 9(b)–9(e)) nucleate above or below the bubbles B4 and B5. It can be expected that the two bubbles will merge with the existing large-size bubbles when they continue to grow. Obviously, the contrast of the overlapping area of helium bubbles is much brighter than that of other areas, which indicates that this area has better light transmittance. The sample thickness is already very thin, and holes will be formed soon. Therefore, the overlap of helium bubbles will greatly accelerate the formation of the microcracks at grain boundaries.

4. Discussion

4.1. Growth behavior of helium bubbles during *in-situ* helium irradiation at 673 K

The bubble growth rate can be described by the equation[37]

$$\frac{\mathrm{d}r}{\mathrm{d}t} = \frac{\Omega}{r + a_0}\left[D_\mathrm{v}\left(C_\mathrm{v} - C_\mathrm{vr}\right) - D_\mathrm{i}\left(C_\mathrm{i} - C_\mathrm{ir}\right) + D_\mathrm{g}C_\mathrm{g}v\right), \quad (1)$$

where r is the radius of helium bubble; t is the irradiation time; $\mathrm{d}r/\mathrm{d}t$ is the growth rate of helium bubble; Ω is the volume

of single vacancy, approximately 3.10×10^{-23} cm^3; a is the lattice constant of Mo and $a=3.143$ Å which is obtained according to XRD spectrum; D_v and D_i are the diffusion coefficients of vacancies and interstitials, respectively; C_v and C_i are the concentrations of vacancies and interstitials, respectively, in the matrix; C_{vr} and C_{ir} are the vacancy concentration and interstitial concentration, respectively, at helium bubble; and D_g is the diffusion coefficient of helium atoms at a certain temperature. The coefficient, C_g, is the concentration of helium atoms, and v is the number of vacancies contained in each He atom. The irradiation temperature in our present work is 673 K, lower than $0.3T_m=858$ K (T_m is the melting point of pure molybdenum, approximately 2860 K). Therefore, the main reason for bubble growth at 673 K is that the newly injected helium atoms and the irradiation-induced new vacancies migrate to the formed helium bubbles during helium irradiation. Of course, helium atoms, vacancies, and H_mV_n clusters already in Mo matrix will also migrate to the formed bubbles, but this is not the main reason. Therefore, the equation (1) can be written as

$$\frac{dr}{dt}=\frac{\Omega}{r+a_0}D_gC_gv. \tag{2}$$

Here D_g[38] can be obtained according to the following equations:

$$D_g=D_0\,e^{-\frac{E_s}{kT}}, \tag{3}$$

$$E_s=Q/2=7.5\times10^{-4}T_m, \tag{4}$$

$$D_0=\alpha\Gamma a_0^2, \tag{5}$$

where α is the geometric factor ($\alpha=1/4$ in BCC structure); a is the jump (length $=a_0/2$); D is the diffusion coefficient of helium atoms; E_s is the surface migration activation energy of Mo; k is the Boltzmann constant; T is the Kelvin temperature; Q is the self-diffusion energy. Γ is the jump frequency, according to the formula proposed by Zener and wert,[39] $\Gamma=\sqrt{2E_s/ma^2}$; m is the mass of helium atom and is 6.64×10^{-27} kg. Therefore, we can obtain the values $E_s=2.16$ eV, $\Gamma=3.25\times10^{13}$ s^{-1}, $D_0=8.03\times10^{-3}$ cm^2/s, and the diffusion coefficient of helium atoms in Mo at 673 K ($D_{g(673\ K)}=8.03\times10^{-3}\times\exp[-2.16/(8.63\times10^{-5}\times673)]=5.57\times10^{-19}$ cm^2/s).

The helium irradiation flux is 6.6×10^{12} ions/cm^2·s and the thickness of the *in-situ* monitored region is approximately 105 nm at 673 K irradiation. Therefore, according to the SRIM simulation results, the helium concentration rate retained in the monitored region is 4.95×10^{-4} at.%/s $=4.95$ appm/s. It should be noted that with the increase of the number of implanted He atoms, the proportion of total atomic weight of helium in Mo matrix cannot be ignored. Therefore, the variation relationship of helium concentration can be calculated as $C_g=(4.95\times10^{-6}t)/(1+4.95\times10^{-6}t)=t/(2.02\times10^5+t)$, where t is the irradiation time in second.

Therefore, the size of helium bubble can be calculated as

$$\frac{dr}{dt}=\frac{1.73\times10^{-34}}{r+0.31}\frac{t}{2.02\times10^5+t}v. \tag{6}$$

The relationship between helium bubble size and irradiation time can be obtained as follows:

$$r=-0.31+\sqrt{9.6\times10^{-2}+3.5\times10^{-34}vt-7.0\times10^{-29}v\ln\left(2.0\times10^5+t\right)+C}. \tag{7}$$

In the above formula, C is a constant, and the vacancy number v of each He atom is a variable parameter related to the irradiation time. Therefore, according to Eq. (7), at 673 K irradiation, we can obtain the bubble size at any irradiation time.

4.2. Growth behavior of helium bubbles during *in-situ* annealing

Figure 10(a) shows the relationship between the size of helium bubble and the annealing time at different annealing temperatures. The experimental results clearly show that the size of helium bubbles increases with the increase of annealing time. The higher the annealing temperature is, the faster the size growth will be. The best fitting formulas of helium bubble size and annealing time at different annealing temperatures are as follows:

$$773\ K: R_{T=773\ K}=1.27\cdot t^{0.12}+0.96, \tag{8}$$

$$873\ K: R_{T=873\ K}=0.858\cdot t^{0.15}+1.9, \tag{9}$$

$$973\ K: R_{T=973\ K}=0.347\cdot t^{0.33}+3.0, \tag{10}$$

where R represents the average size of helium bubbles in units of nm and t is the annealing time in second.

According to Eqs. (8)–(10), the general rule of helium bubble growth during annealing can be obtained as $R=A\cdot t^n+R_0$, where R_0 represents the original average size of helium bubble before annealing. Fox example, in the present work, R_0 is the average size of helium bubble after irradiation with a fluence of 5.74×10^{16} ions/cm^2 at 673 K when annealing begins at 673 K. Figure 10(b) shows the fitting relationships between coefficient A, exponent n and annealing temperature according to Eqs. (8)–(10),

$$A=-1.39\times10^{-4}\exp(T/108.5)+1.44, \tag{11}$$

$$n=2.91\times10^{-4}\exp(T/137.4)-0.0176, \tag{12}$$

where T is the annealing temperature in K. Therefore, the average size of helium bubbles can be estimated for any annealing time at a certain annealing temperature.

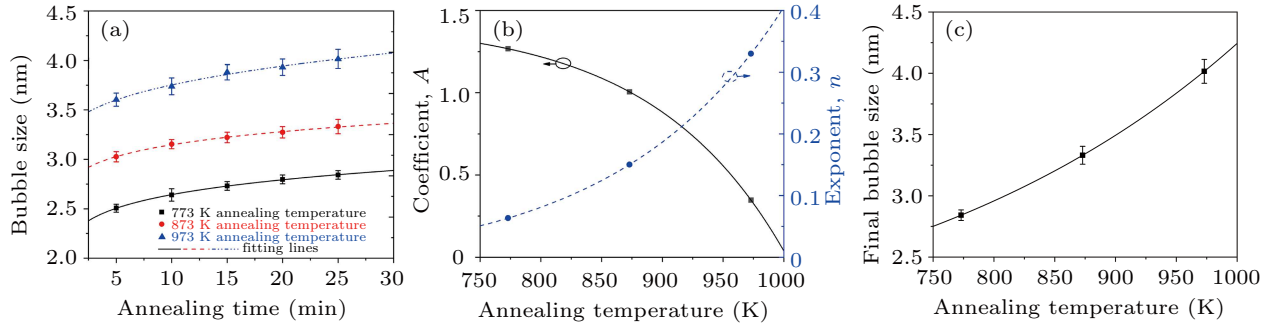


Fig. 10. (a) The relationship between the size of helium bubbles and annealing time under different annealing temperatures. (b) The relationship between the coefficient exponents in the bubble growth equation and annealing temperatures. (c) The relationship between the final average size of helium bubbles and annealing temperature.

Figure 10(c) shows the relationship between the final average size of helium bubbles and annealing temperature. It can be seen that with the increase of annealing temperature, the increase speed of the final average size of helium bubble is accelerated. At the same annealing time, we observe that in the current 673–873 K annealing, when the temperature is increased by one level, helium bubble can rapidly increase to a size saturation, and then prolonging the annealing time, its size change is not obvious. Gan *et al.*[40] reported that the arrangement of bubble superlattice was observed in the Mo irradiated by 40 keV He^+ with the fluence of 1×10^{17} ions/cm^2 at 573 K. After the *in-situ* heating at 1123 K, the superlattice structure remained stable, and the size of helium bubbles did not significantly increase. This indicates that the helium concentration may be the main reason limiting the growth of helium bubbles.

The growth mechanisms of gas bubbles in a solid include (i) first mechanism: the movement of newly injected gas atoms and newly created vacancies to previous bubbles, (ii) second mechanism: the diffusion of the undissolved gas atoms and vacancies to previous bubbles, and (iii) third mechanism: the migration of bubbles and coalescence with other bubbles. There are no newly injected helium atoms and new displacement damage in the annealing process. Meanwhile, the solubility of helium atom in Mo is very low. The first mechanism needs the introduction of new helium atoms and vacancies. Therefore, the growth of helium bubbles should be attributed to the second and third mechanisms, in which vacancies, helium atoms, and defect clusters (small-sized helium bubbles) migrate to the existing bubbles and the bubbles aggregate under the thermal effect, resulting in bubble growth. There are two ways of migration and coalescence of helium bubbles in the annealing process: surface diffusion and volume diffusion. Surface diffusion is an important mechanism for the irregular movement of bubbles in solids. Since the thickness of the monitored region in our experiment is only 105 nm at 673 K irradiation, the growth of helium bubbles is dominated by surface diffusion. Since the motion of bubbles is random, the diffusion coefficient of helium bubbles during annealing can be described by the following equation according to the dynamics of surface diffusion:[41]

$$D_{\rm b} = 3\Omega^{4/3}/2\pi R^4 \cdot D_{\rm s}, \tag{13}$$

where $D_{\rm s}$ is the surface diffusion coefficient, and the calculation formula is as follows:

$$D_{\rm s} = D_0\, {\rm e}^{-\frac{E_{\rm S}}{kT}}, \tag{14}$$

with $D_0 = 8.03\times10^3$ cm^2/s, therefore,

$$D_{\rm s} = 8.03\times10^{-3}\exp(-25058T), \tag{15}$$

$$D_{\rm b} = 3.69\times10^{-32}/R^4\exp(-25058T). \tag{16}$$

According to the final size $R_{\rm f}$ of helium bubbles obtained by the experiment and the values of $D_{\rm s}$ and $D_{\rm b}$ at different annealing temperatures obtained according to formulas (15) and (16) are shown in Table 2. The influence factors of $D_{\rm b}$ include the size of helium bubbles and annealing temperature. Because the size of helium bubbles changes a little in our work, the annealing temperature is the main factor. Therefore, the higher the temperature is, the higher the $D_{\rm b}$ value will be.

Table 2. The $R_{\rm f}$, $D_{\rm s}$ and $D_{\rm b}$ at different annealing temperatures.

Temperature (K)	773	873	973
$R_{\rm f}$ (cm)	1.42×10^{-7}	1.67×10^{-7}	2.01×10^{-7}
$D_{\rm s}$ (cm$^2\cdot$s^{-1})	6.70×10^{-17}	2.75×10^{-15}	5.25×10^{-14}
$D_{\rm b}$ (cm$^2\cdot$s^{-1})	7.59×10^{-19}	1.64×10^{-17}	1.48×10^{-16}

4.3. Formation of polyhedral bubbles at 1173 K irradiation

It is a common feature that bubbles evolve into nonspherical polyhedral geometry at high temperature, typically platelet bubbles in hexagonal close-packed (HCP) structure (such as SiC,[42] Ti,[43] and Zr[44]) and octahedral bubbles in face-centered cubic (FCC) structure (such as Cu and Au[23]). The appearance of nonspherical polyhedral bubbles shows that the growth of helium bubbles is not homogeneous, but two-dimensional along the plane with obvious preferred orientation. In our experiment, the cubic structure of helium bubbles in the high-temperature irradiated Mo (BCC) indicates that they have a similar preferential orientation with edges parallel to the {001} habit planes. The gas pressure inside a bubble

is an important factor affecting its shape and energy, which is significantly affected by the temperature.[25] At low temperature, the unsaturated state cannot overcome the repulsive force between the matrix and the bubble, resulting in the bubble to deform uniformly and become spherical. This means a balance between bubble pressure and spherical bubble surface tension, and there is no elastic strain energy in the lattice near the bubble.[45] While at high temperature, the overpressure bubble tends to decrease the extra elastic strain energy stored in the lattice, which can be achieved by preferentially forming a large area face on the low energy plane.[46] Therefore, in terms of system energy, helium bubbles tend to form polyhedral bubbles with low energy at high temperature, rather than spherical bubbles with high surface energy. In addition, Wei *et al.*[23] considered that the increase of crystal surface area should also satisfy Gibbs–Wulff crystal growth model when the crystal recedes due to bubble growth, that is, the shape of helium bubble is determined by the crystal plane with the minimum surface energy. And they also observed octahedral bubbles surrounded by {111} planes in Au and Cu after pre-irradiation and then annealing, which is due to the lowest surface energy of {111} planes in the FCC structure. In our case, Mo is a typical BCC structure, and the {100} planes have the lowest surface energy. Therefore, to minimize the system energy, helium atoms preferentially arrange on the {100} planes by surface diffusion during the growth of helium bubble. Tyler *et al.*[47] first discovered the bubbles with the shape of tetrakaidodecahedra in Nb alloys (BCC structure), and then after the long-time annealing, the {110} facets would gradually disappear and the bubbles would eventually develop into a cubic shape bounded by {100} planes. This also proves that the polyhedral bubbles in BCC materials prefer to grow in a shape bounded by {100} planes where the surface energy is minimum.

5. Conclusions

In this work, the evolution of helium bubbles in purity Mo was studied by *in-situ* TEM observation during 30 keV He^+ irradiation and post-implantation annealing. The main conclusions could be made as followings:

(i) At 673 K irradiation, when helium concentration was 0.89 at.%, many helium bubbles with the average size of 1.38 nm were observed. The size of helium bubbles increased slowly from 1.56 nm to 2.28 nm as the helium concentration increased from 1.19 at.% to 4.31 at.%. During the whole irradiation process, the average size of helium bubble only increased by 0.9 nm from visible state to the end of irradiation. The growth mechanism of helium bubbles was that the new helium atoms and vacancies introduced by irradiation migrated into the existing bubbles. Based on the experimental results, an empirical formula for calculating the size of helium bubbles with the increase of irradiation time was obtained by modifying the theoretical formula.

(ii) After annealing at 773 K, 873 K and 973 K for 25 min, the average sizes of helium bubbles were 2.5 nm, 2.8 nm and 3.3 nm, respectively. The formulas for calculating the average size of helium bubbles during the annealing were as follows: 773 K: $R_{T=773\ \mathrm{K}} = 1.27 \cdot t^{0.12} + 0.96$; 873 K: $R_{T=873\ \mathrm{K}} = 0.858 \cdot t^{0.15} + 1.9$; 973 K: $R_{T=973\ \mathrm{K}} = 0.347 \cdot t^{0.33} + 3.0$.

(iii) The grain boundaries were strong defect sinks, which could effectively absorb the implanted helium atoms and irradiation vacancies and form large-size helium bubbles under high temperature irradiation (1173 K). A denuded zone was formed near the grain boundary, but its width decreased with the increase of irradiation dose. The implanted helium atoms tended to gather at the nucleated bubbles rather than nucleated independently, especially at the grain boundaries. The overlap of helium bubbles would greatly accelerate the formation of the microcracks at grain boundaries.

(iv) Compared with the results at low-temperature *in-situ* irradiation and subsequent annealing experiments, the bubble size under high-temperature irradiation increased dramatically, and the geometry of helium bubbles changed from sphericity to polyhedron. The polyhedral bubbles preferred to grow in a shape bounded by {100} planes where the surface energy was minimum.

Acknowledgement

The authors would like to acknowledge Zhehui Zhou and Jinchi Huang from the Xiamen University for the support of TEM experiments and ion irradiation experiments, respectively.

References

[1] Yvon P and Carre F 2009 *J. Nucl. Mater.* **385** 217
[2] Tavassoli A A F 2002 *J. Nucl. Mater.* **302** 73
[3] Wu G Y, Hu N W, Deng H Q, Xiao S F and Hu W Y 2017 *Nucl. Sci. Tech.* **28** 29
[4] Gao N, Shen T L, Kurtz R, Wang Z G and Gao F 2016 *Scr. Mater.* **113** 190
[5] El-Atwani O, Aydogan E, Esquivel E, Efe M, Wang Y Q and Maloy S A 2018 *Acta Mater.* **147** 277
[6] Marian J, Wirth B D and Perlado J M 2002 *Phys. Rev. Lett.* **88** 255507
[7] Arakawa K, Hatanaka M, Kuramoto E, Ono K and Mori H 2006 *Phys. Rev. Lett.* **96** 125506
[8] Li B S, Yang Z, Xu S, Wei K F, Wang Z G, Shen T L, Zhang T M and Liao Q 2021 *Chin. Phys. B* **30** 36102
[9] Li Y P, Wang L, Ran G, Yuan Y, Wu L, Liu X Y, Qiu X, Sun Z P, Ding Y F, Han Q, Wu X Y, Deng H Q and Huang X Y 2021 *Acta Mater.* **206** 116618
[10] El Keriem M S A, Van Der Werf D P and Pleiter F 1993 *Phys. Rev. B* **47** 14771
[11] Gilbert M R and Sublet J C 2011 *Nucl. Fusion* **51** 043005
[12] Xu W Z, Zhang Y F, Cheng G M, Jian W W, Millett P C, Koch C C, Mathaudhu S N and Zhu Y T 2013 *Nat. Commun.* **4** 2288
[13] Dennett C A, So K P, Kushima A, Buller D L, Hattar K and Short M P 2018 *Acta Mater.* **145** 496

[14] Xie H X, Gao N, Xu K, Lu G H, Yu T and Yin F X 2017 *Acta Mater.* **141** 10
[15] Wang L, Hao T, Zhao B L, Zhang T, Fang Q F, Liu C S, Wang X P and Cao L 2018 *J. Nucl. Mater.* **508** 107
[16] Liao Q, Li B S, Kang L and Li X G 2020 *Chin. Phys. B* **29** 076103
[17] Shehla H, Ali A, Zongo S, Javed I, Ishaq A, Khizar H, Naseem S and Maaza M 2015 *Chin. Phys. Lett.* **32** 096101
[18] Ono K, Arakawa K and Hojou K 2002 *J. Nucl. Mater.* **307** 1507
[19] El-Atwani O, Cunningham W S, Perez D, Martinez E, Trelewicz J R, Li M and Maloy S A 2020 *Scr. Mater.* **180** 6
[20] Yi X O, Arakawa K, Nguyen-Manh D, Ferroni F, Liu P, Han W, Wan F and Roberts S G 2017 *Fusion Eng. Des.* **125** 454
[21] Chen Y, Li Y P, Ran G, Wu L, Ye C, Han Q, Wang H and Du H L 2020 *Prog. Nucl. Energy* **129** 103502
[22] Wand H J, Li Y D, Guo Q, Ma L Y, Wen L and Wang B 2015 *Chin. Phys. Lett.* **32** 056102
[23] Wei Q M, Li N, Sun K and Wang L M 2010 *Scr. Mater.* **63** 430
[24] Tyler S K and Goodhew P J 1983 *Radiat. Eff.* **78** 147
[25] Yan Z F, Yang T F, Lin Y R, Lu Y P, Su Y, Zinkle S J and Wang Y G 2020 *J. Nucl. Mater.* **532** 152045
[26] Li R R, Zhang Y F, Geng D C, Zhang G W, Watanabe H, Han W T and Wang F R 2019 *Acta Phys. Sin.* **68** 216101 (in Chinese)
[27] Zhang J C, Sun S, Yang Z M, Qiu N and Wang Y 2020 *Chin. Phys. B* **29** 066104
[28] Li F B, Ran G, Gao N, Zhao S Q and Li N 2019 *Chin. Phys. B* **28** 085203
[29] Wang D, Gao N, Setyawan W, Kurtz R J, Wang Z G, Gao X, He W H and Pang L L 2016 *Chin. Phys. Lett.* **33** 096102
[30] Lane P and Goodhew P 1983 *Philos. Mag. A* **48** 965
[31] El-Atwani O, Hinks J A, Greaves G, Allain J P and Maloy S A 2017 *Mater. Res. Lett.* **5** 343
[32] Li Y P, Ran G, Guo Y J, Sun Z P, Liu X Y, Li Y M, Qiu X and Xin Y 2020 *Acta Mater.* **201** 462
[33] Huang M J, Li Y P, Ran G, Yang Z B and Wang P H 2020 *J. Nucl. Mater.* **538** 152240
[34] Ziegler J F, Ziegler M D and Biersack J P 2010 *Nucl. Instrum. Methods Phys. Res. Sect. B Beam Interact. Mater. Atoms* **268** 1818
[35] *Standard Practice for Neutron Radiation Damage Simulation by Charge-Particle Irradiation* E521-96, Annual Book of ASTM Standards, Vol. 12.02, American Society for Testing and Materials, Philadelphia (1996) Reapproved 2009
[36] Zhang W P, Luo F F, Yu Y X, Zheng Z C, Shen Z Y, Guo L P, Ren Y Y and Suo J P 2016 *J. Nucl. Mater.* **479** 302
[37] Was G S 2016 *Fundamentals of Radiation Materials Science: Metals and Alloys,* 2nd edn (New York: Springer) pp. 467–469
[38] Evans J 2004 *J. Nucl. Mater.* **334** 40
[39] Frauenfelder R 1969 *J. Vac. Sci. Technol.* **6** 388
[40] Gan J, Sun C, He L F, Zhang Y F, Jiang C and Gao Y P 2018 *J. Nucl. Mater.* **505** 207
[41] Kelly R 1967 *Phys. Status Solidi* **21** 451
[42] Chen P J J and Trinkaus H 1999 *Phys. Rev. Lett.* **82** 2709
[43] Schober T and Trinkaus H 1992 *Philos. Mag. A* **65** 1235
[44] Miller W A, Carpenter G J C and Chadwick G A 1969 *Philos. Mag.* **19** 305
[45] Trinkaus H and Singh B N 2003 *J. Nucl. Mater.* **323** 229
[46] Goodhew P J 1981 *J. Nucl. Mater.* **98** 221
[47] Tyler S K and Goodhew P J 1979 *J. Microsc.* **116** 55